# Diamond ascent by rift-driven disruption of cratonic mantle keels

Thomas M. Gernon[a,*], Stephen M. Jones[b], Sascha Brune[c,d], Thea K. Hincks[a], Anne Glerum[c,d], Martin R. Palmer[a], John C. Schumacher[e], Rebecca M. Primiceri[a], Matthew Field[f], William L. Griffin[g], Suzanne Y. O'Reilly[g], Derek Keir[a,h], Christopher J. Spencer[i], Andrew S. Merdith[j]

[a] *School of Ocean & Earth Science, University of Southampton, Southampton SO14 3ZH, UK*
[b] *School of Geography, Earth & Environmental Sciences, University of Birmingham, Edgbaston, Birmingham B15 2TT, UK*
[c] *Helmholtz Centre Potsdam – GFZ German Research Centre for Geosciences, Potsdam, Germany*
[d] *University of Potsdam, Potsdam-Golm, Germany*
[e] *Department of Geology, Portland State University, Portland, OR, USA*
[f] *Mayfield, Wells Road, Wookey Hole Wells, Somerset, BA5 1DN, UK*
[g] *GEMOC ARC National Key Centre, Earth and Environmental Sciences Macquarie University NSW 2109, Australia*
[h] *Dipartimento di Scienze della Terra, Universita degli Studi di Firenze, Florence, Italy*
[i] *Department of Geological Sciences and Geological Engineering, Queen's University, Kingston, Canada*
[j] *School of Earth and Environment, University of Leeds, Leeds LS2 9TJ, UK*

---

# Extended Data Figures and Tables

**This PDF file includes:**

Extended Data Figures 1–9

Extended Data Table 1

References are provided in the Methods.

*Corresponding author: Thomas.Gernon@noc.soton.ac.uk

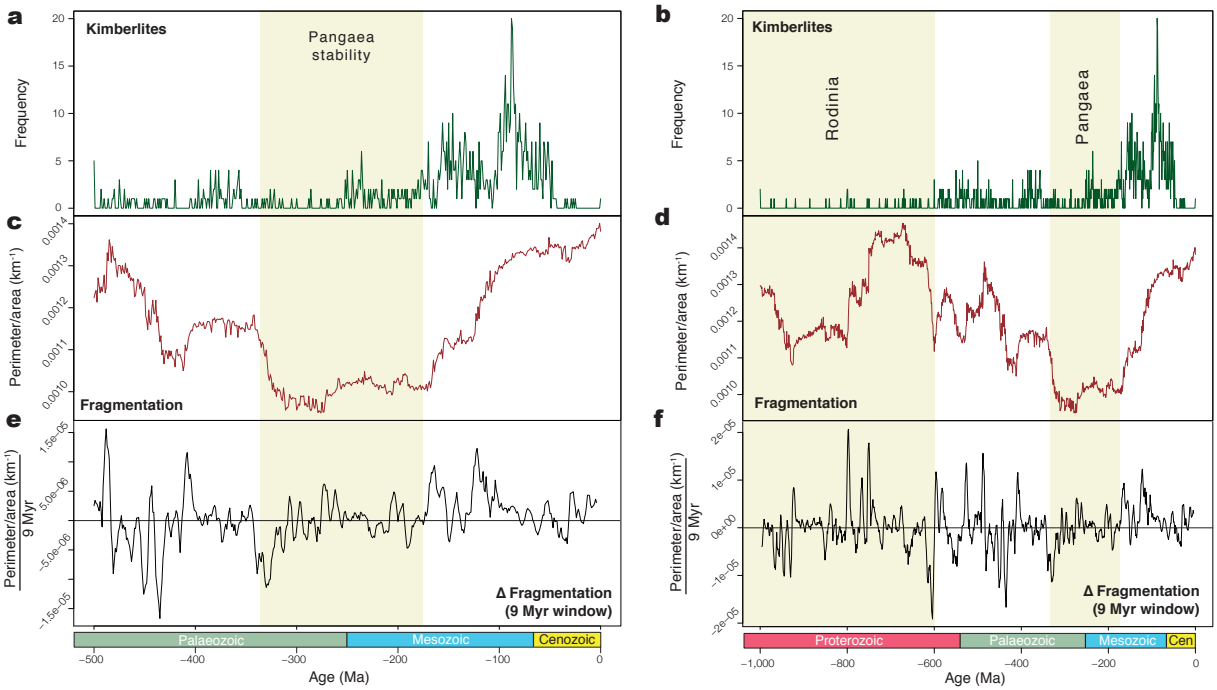


**Extended Data Figure 1. Relationship between continental fragmentation and global kimberlites | a,** Kimberlite distribution since 500 Ma (N=860) and **b,** since 1 Ga (N=981), using well-dated kimberlites from the compilation of ref.[6]. **c,** Continental fragmentation (continental perimeter/area) derived from paleogeographic reconstructions of ref.[16] for 500–0 Ma and **d,** 1000–0 Ma. **e,** Rate of change of continental fragmentation ($\Delta F$; Methods) using a 9 Myr window for 500–0 Ma and **f,** 1000–0 Ma

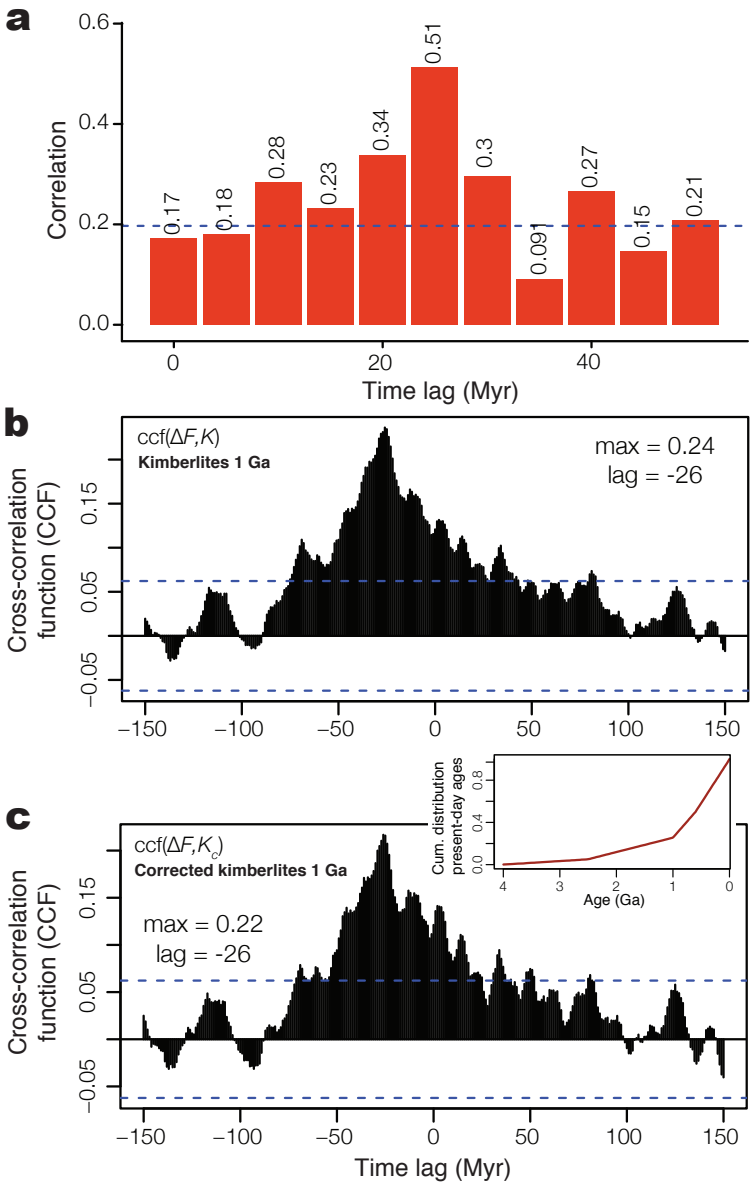


**Extended Data Figure 2. Relationship between dynamic continental fragmentation and global kimberlites | a,** Conditional correlations for $\Delta F$ (slope over 9 Myr moving window) and kimberlites (count) for the period 500–0 Ma, calculated using a Bayesian network[17] (Methods). Here, the input is a 5 Myr resolution series, where kimberlite count is the total number of events in each 5 Myr interval, and $\Delta F$ is the slope of the regression line for fragmentation estimated every 5 Myr. Using a simple saturated BN (where each node is linked by an arc to every other node in the network) we computed the correlation of $\Delta F$ and kimberlite count $corr(\Delta F, K)$; then the correlation of $\Delta F$ and kimberlite with a lag of 5 Myr (where $\Delta F$ precedes kimberlites) conditional on $\Delta F$ (unlagged); i.e., $corr(\Delta F_{t-5}, K \mid \Delta F)$; then the correlation at lag 10 Myr, conditional on the lags at 0 and 5 Myr $corr(\Delta F_{t-10}, K \mid \Delta F, \Delta F_{t-5})$ etc., up to a lag of 50 Myr. This removes the effect of shorter lags, and thus the effects of autocorrelation in the individual processes. Note that this test confirms that the maximum correlation between continental fragmentation and kimberlites occurs at a lag of ~25 Myr after fragmentation (with uncertainty of approximately ±4 Myr). **b,** Cross-correlations between kimberlites[6] (n=981) and the rate of change of tectonic fragmentation ($\Delta F$; 9 Myr window) spanning 1 Ga (Methods), showing dominant time lags at –26 ± 4 Myr (i.e., fragmentation preceding kimberlites); the dashed blue lines show the 95% confidence intervals. **c,** Cross-correlations between kimberlites and $\Delta F$ accounting for potential preservation bias in the record by weighting kimberlite distributions inversely according to surface preservation (shown in inset from ref.[75]). Note that this analysis does not affect the dominant time lag (–26 Myr) relative to (**b**).

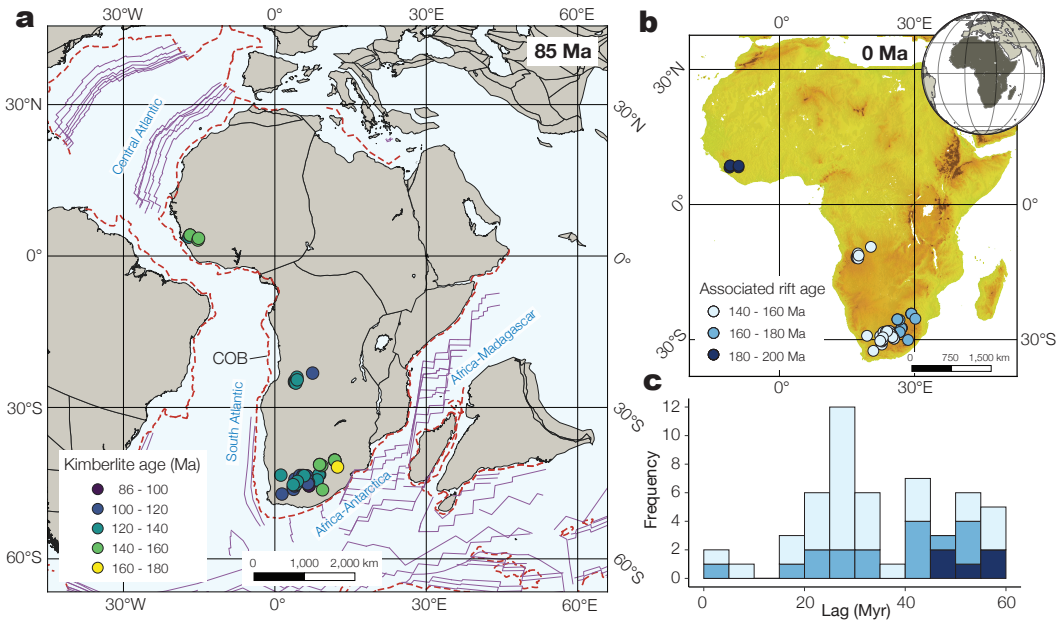


**Extended Data Figure 3. Location and context of Mesozoic kimberlites in Africa at 85 and 0 Ma | a,** Plate tectonic reconstruction at 85 Ma (constructed using GPlates[51]; https://www.gplates.org/) showing the location of kimberlites from the regional case study (Fig. 1c) with respect to inferred continent ocean boundaries (COB)[51]. The kimberlites are coloured by their radiometric ages[6]. **b,** Location of kimberlites at the present-day coloured by the age of the closest rift system in space and time (Methods).

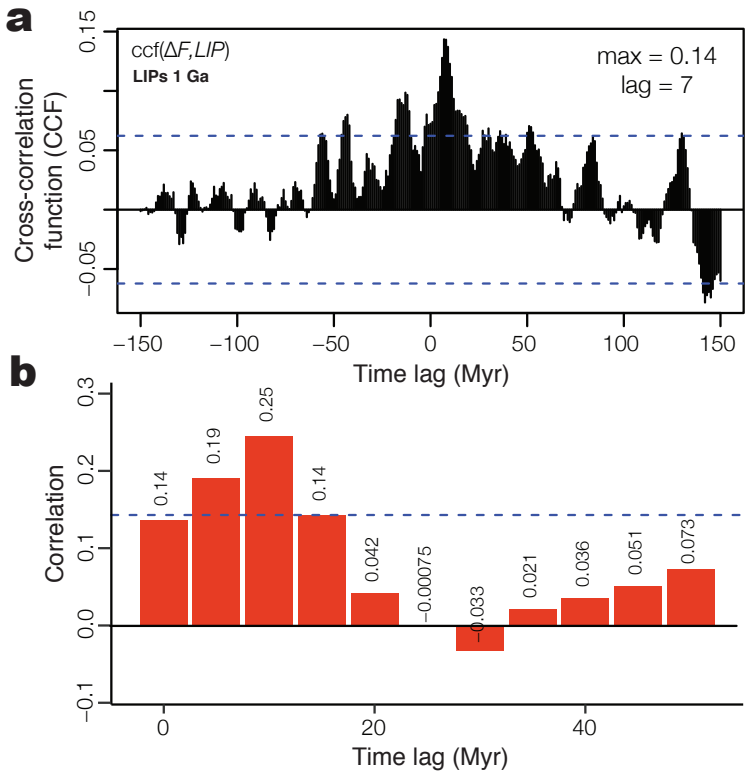


**Extended Data Figure 4. Relationship between dynamic continental fragmentation and plumes over 1 Ga | a,** Cross-correlations between $\Delta F$ (9 Myr window) and plumes over 1 Ga, using the well-established ages of their surface expression, large igneous provinces (LIPs)[24] (n=104). This analysis reveals a strong peak at +7 ± 4 Myr lags, indicating that the onset of LIP magmatism most commonly occurs ~7 Myr before continental fragmentation. **b,** Results of a Bayesian network investigating the link between LIPs and $\Delta F$, and configured for LIPs leading $\Delta F$ (as shown in (**a**) to be dominant). The input is a 5 Myr resolution series, where LIP is the total number of LIP events with a start date falling in each 5 Myr interval, and $\Delta F$ is the slope of the regression line for fragmentation (over a 9 Myr window) estimated every 5 Myr. Critically, this analysis removes the effect of shorter lags, and thus the effects of autocorrelation in the individual processes. The maximum conditional correlation is 0.25 and occurs at a lag of ~10 ± 4 Myr (where LIP leads $\Delta F$). The dashed blue line shows the estimated 95% confidence interval (threshold for the 95% CI = 0.143 for the 5 Myr resolution time series of length n = 188).

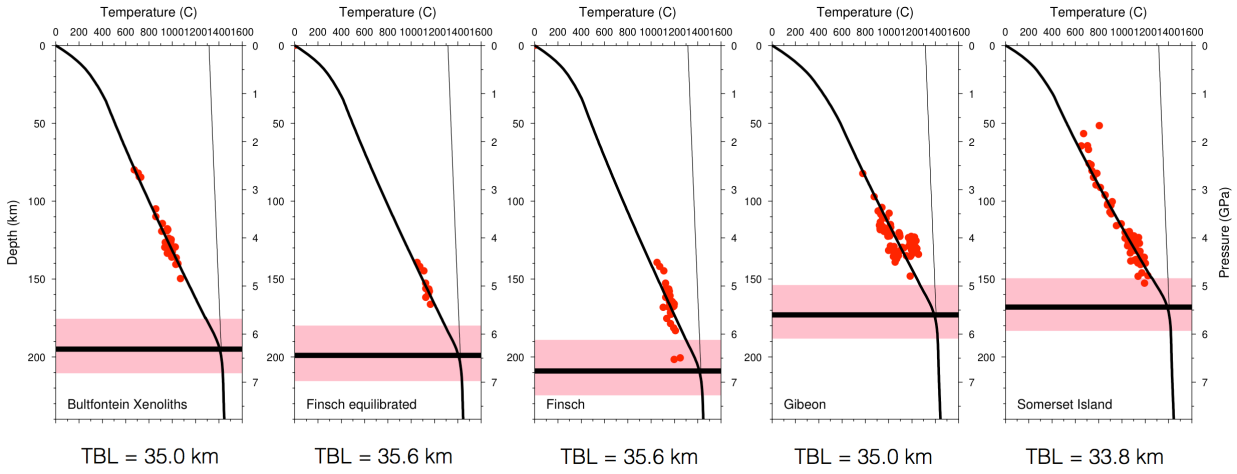


**Extended Data Figure 5. Thermal boundary layer properties derived from xenolith geotherms** | Thickness and temperature conditions of the lower lithospheric thermal boundary layer (TBL) derived using peridotite xenolith-*P*-*T*-based geotherms of Mather et al. (2011)[53] for four different kimberlites: Bullfontein, Finch, Gibeon and Somerset Island (Methods). Note that the TBL is consistently ~35 km thick, with an estimated temperature range of 1,298 to 1,436°C. At pressures of 5–7 GPa, these temperature conditions straddle the carbonate melt solidus, conditions that are capable of generating carbonate-rich partial melts (Fig. 3b). Also note that thickness is very similar to the amount (30–40 km) which is thought to have delaminated during the Mesozoic emplacement of kimberlite fields across the Kaapvaal Craton of southern Africa (see Extended Data Fig. 9), suggesting that the TBL is entirely removed.

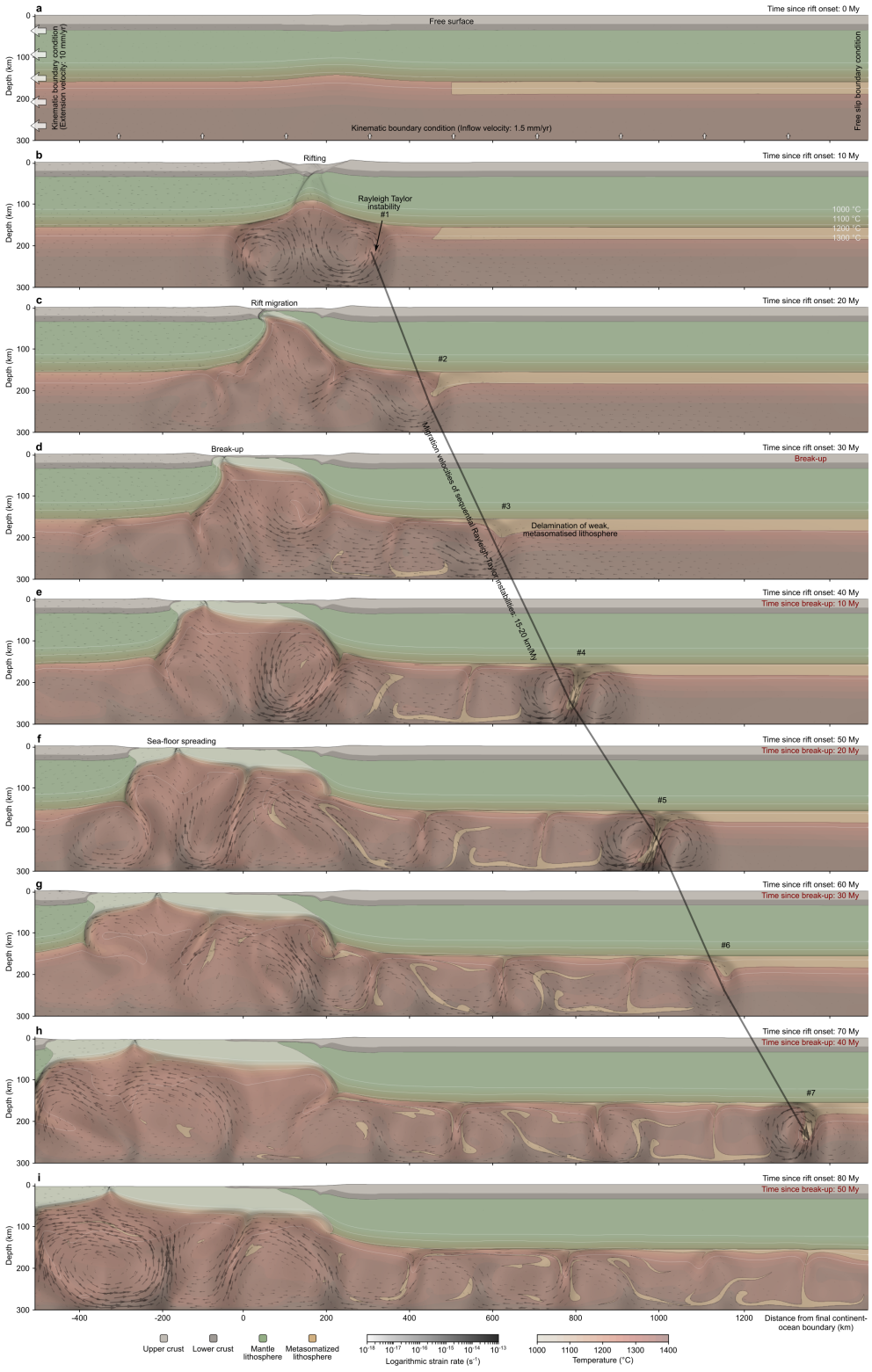


**Extended Data Figure 6. Thermo-mechanical simulations of continental breakup** |. (**a**)–(**i**) Generation and propagation of sequential Rayleigh-Taylor instabilities (labelled 1–7 at different time slices), which overall exhibit migration velocities of 15–20 km Myr$^{-1}$.

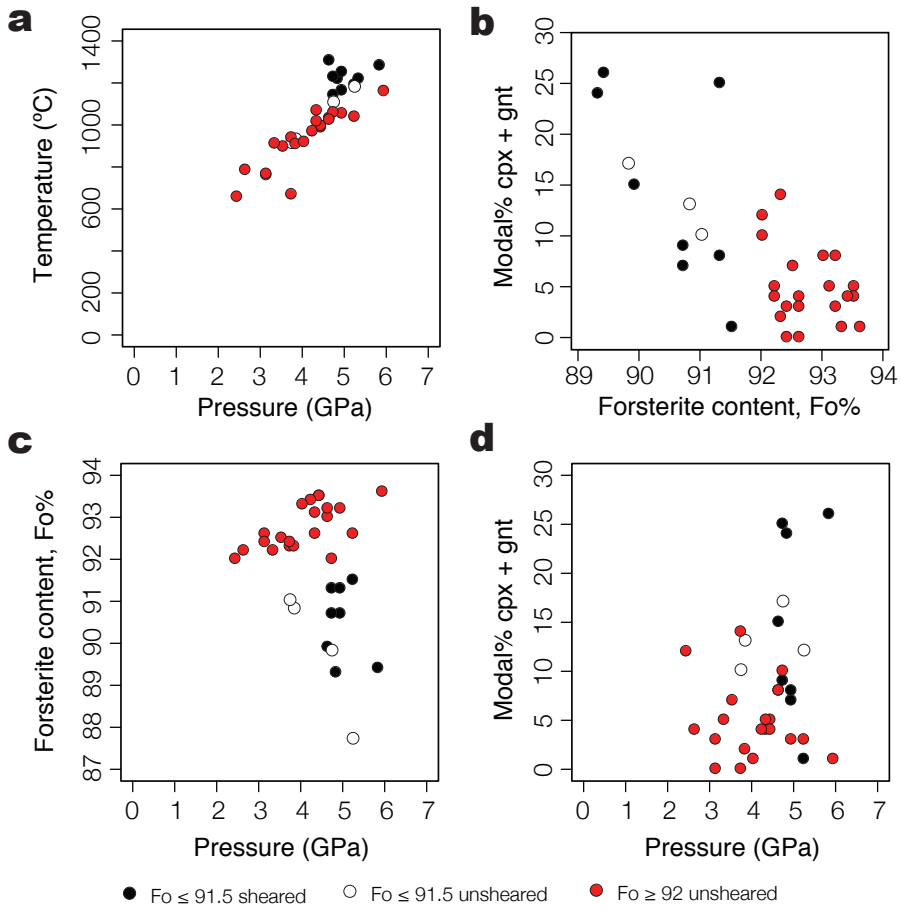


**Extended Data Figure 7. Compositional and *P-T* characteristics of southern African xenoliths, showing the effects of refertilization | a,** Pressure versus temperature estimates (from thermometry and barometry) of peridotite xenoliths from the Kaapvaal Craton (data are from various sources summarised in ref.[30]); note that the majority of low-Fo xenoliths lie above the geotherm defined by high-Fo xenoliths and are sheared, providing good evidence of a thermal effect. **b,** Olivine forsterite content (Fo%) versus modal % clinopyroxene + garnet (as a measure of fertility); note the negative correlation of Fo with fertility. **c,** Pressure versus Fo; note the concentration of low-Fo xenoliths between 4.5–5.2 GPa (~22 km thick), interpreted to represent a dense boundary layer. **d,** Pressure versus modal % cpx+gnt; note the general high fertility of low-Fo xenoliths—with two-thirds containing cpx+gnt >10.

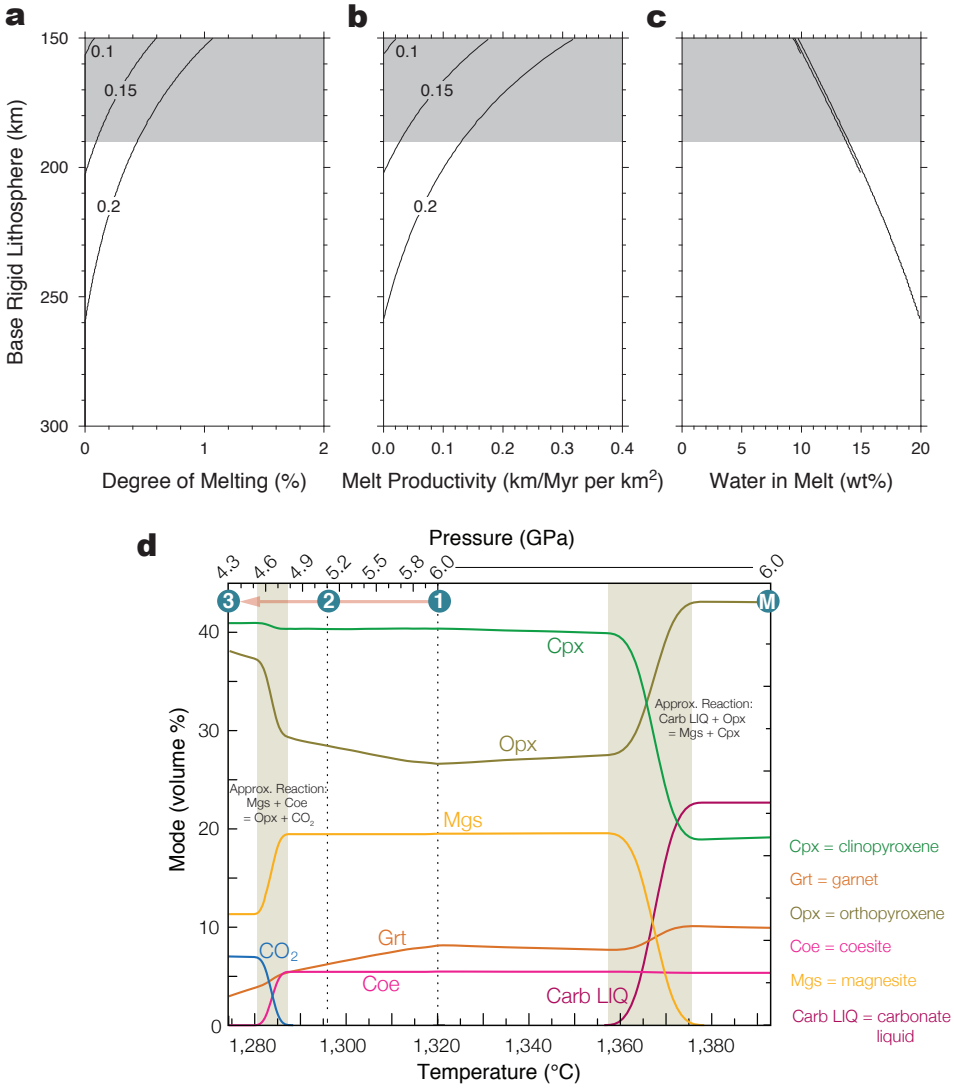


**Extended Data Figure 8. Conditions of kimberlite melt generation and ascent | a,** Degree of melting as a function of depth to the base of the rigid lithosphere (i.e., mechanical boundary layer); **b,** the associated melt productivity per unit area of convective upwelling, assuming a mean upwelling rate of 30 km/Myr determined from the numerical models (Fig. 2), and **c,** the wt% water in the melt for bulk water contents of 0.1, 0.15 and 0.2 wt% (annotated on the curves); calculations use the hydrous decompressional melting parameterisation of ref.[64] (see Methods for further details); **d,** Modelled phase modes for starting composition JADSCM-7[27] along a *P–T* path shown (points 1–3) in Fig. 3b. The approximate reactions are shown; note the occurrence of $CO_2$ exsolution below pressures of ~5 GPa.

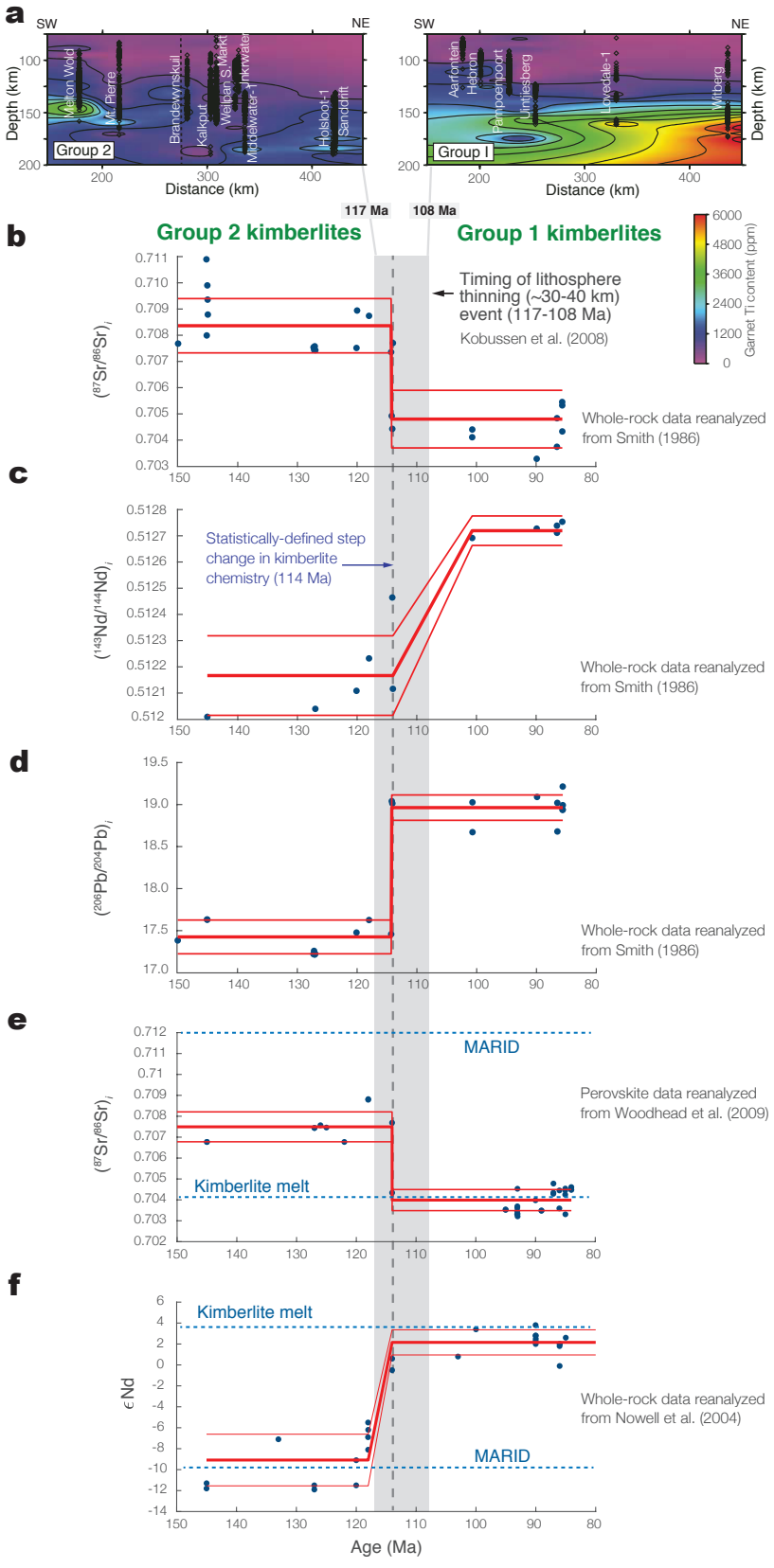


**Extended Data Figure 9.** (Continued on the following page.)

**Extended Data Figure 9.** (preceding page) **Changing chemistry of kimberlites in the Kaapvaal Craton from 150–85 Ma** | **a,** Interpolated plots of Ti contents of garnet xenocrysts (modified after ref.[40]) at 117 Ma (left) and 108 Ma (right), showing the effects of heating and chemical refertilization of the lower lithosphere by asthenospheric melts, ultimately thinning the lithosphere by 30–40 km (shown as the vertical grey field). Below this are the chemical compositions of Group 2 and Group 1 kimberlites, specifically whole-rock $(^{87}Sr/^{86}Sr)_i$ (**b**), whole-rock $(^{143}Nd/^{144}Nd)_i$ (**c**), and whole-rock $(^{206}Pb/^{204}Pb)_i$ (**d**); these data are updated from Smith (1986)[47]. **e,** $(^{87}Sr/^{86}Sr)_i$ of kimberlitic perovskites from Woodhead et al. (2009)[70]. The plot shows the MARID (Mica-Amphibole-Rutile-Ilmenite-Clinopyroxene) end-member defined from kimberlite xenoliths and thought to derive from a lithospheric mantle source[72]; and a kimberlite melt end-member[72] largely defined from analyses of PIC (Phlogopite-Ilmenite-Clinopyroxene) kimberlite xenoliths. **f,** Whole-rock $\epsilon$Nd calculated from the data of Nowell et al. (2004)[71]. The lines on the plots show the statistically defined change points (using conjugate partitioned recursion; see Methods) and two-sigma uncertainty bounds of the two averages (thin red lines) before and after the change point. Note that the step changes occur at 114 Ma for all variables, except $(^{143}Nd/^{144}Nd)_i$, which occurs between 114–100 Ma, and $\epsilon$Nd, which occurs between 118–114 Ma. The dashed vertical line shows the most prominent step change in compositions at 114 Ma. Note that continent-scale metasomatism occurred before 114 Ma[44], raising the possibility that migrating chains of Rayleigh-Taylor instabilities (Fig. 2) partially melted asthenosphere and lithosphere, driving infiltration of the resulting carbonated melts into the lowermost lithosphere, thus causing widespread melt-metasomatism that further destabilized cratonic keels.

**Extended Data Table 1: Rayleigh-Taylor instability models applied to lithospheric root delamination**. **a,** Six analytical models describe two fluid layers where the upper layer has the higher density (see Methods). The models differ in the relative layer thicknesses, viscosity and vertical density gradient. The models are specified in terms of a scaled dominant wavelength $b^*$ and a corresponding scaled exponential growth rate $q^*$. Actual wavelengths and e-folding growth times are shown for a lithospheric thermal boundary layer (upper layer) of 25 km with a temperature increase of 250°C and a viscosity of $10^{16}$ $m^2/s$. The lateral propagation rate for a chain of instabilities is defined in equation 1 (main paper). The thermal Péclet number for vertical return flow confirms that asthenosphere will well up adiabatically to replace the removed part of cratonic keel.

**a**

| Key | Model | Scaled Wavelength | Scaled Growth Rate | Instability Wavelength km | Instability Growth Time Myr | Lateral Propagation km/Myr | Upwelling Rate km/Myr | Peclet Number | Reference |
|---|---|---|---|---|---|---|---|---|---|
| 1 | Layer over half-space of same viscosity | 3.7 | 0.097 | 93 | 2.6 | 35 | 1800 | 1426 | 34 |
| 2 | Layer over layer of same thickness and viscosity | 2.6 | 0.077 | 64 | 3.3 | 20 | 867 | 687 | 76 |
| 3 | Layer over much less viscous half-space | 3.0 | 0.160 | 75 | 1.6 | 47 | 1183 | 938 | 34 |
| 4 | Layer with linearly decreasing density over half-space of constant density and same viscosity | 2.9 | 0.037 | 73 | 3.4 | 21 | 1106 | 876 | 34 |
| 5 | space of constant density and much lower viscosity | 2.4 | 0.059 | 60 | 2.1 | 28 | 757 | 600 | 34 |
| 6 | Plastic layer over plastic half-space | 2.8 | 0.610 | 70 | 0.4 | 168 | 1031 | 817 | 34 |

| | |
|---|---|
| 25 | Thermal boundary layer thickness (km) |
| 250 | Thermal boundary layer temperature increase (°C) |
| 1E+16 | Kinematic viscosity ($m^2/s$) |
| 1E-06 | Thermal diffusivity ($m^2/s$) |
| 4E-05 | Thermal expansion coefficient (/°C) |
| 10 | Gravity ($m/s^2$) |
| 0.05 | Reduced Gravity ($m/s^2$) |
| 3E+13 | Seconds per Myr |

**Extended Data Table 1:** Rayleigh-Taylor model parameters (continued) **b,** *ASPECT* model parameters for thermo-mechanical simulations (see Methods). Abbreviations: dis – dislocation creep, diff – diffusion creep.

**b**

| Parameter | Symbol | Units | Upper crust | Lower crust | Lithospheric mantle | Asthenosphere |
|---|---|---|---|---|---|---|
| **Reference density (at surface conditions)** | $\rho_0$ | $kg\ m^{-3}$ | 2700 | 2850 | 3280 | 3300 |
| **Thermal expansivity** | $\alpha$ | $K^{-1}$ | $2.7\cdot10^{-5}$ | $2.7\cdot10^{-5}$ | $3.0\cdot10^{-5}$ | $3.0\cdot10^{-5}$ |
| **Thermal diffusivity** | $\kappa$ | $m^2\ s^{-1}$ | $7.72\cdot10^{-7}$ | $7.31\cdot10^{-7}$ | $8.38\cdot10^{-7}$ | $8.33\cdot10^{-7}$ |
| **Heat capacity** | $C_p$ | $J\ kg^{-1}\ K^{-1}$ | 1200 | 1200 | 1200 | 1200 |
| **Heat production** | $H$ | $W\ m^{-3}$ | $1.0\cdot10^{-6}$ | $0.1\cdot10^{-6}$ | 0 | 0 |
| | | | | | | |
| **Cohesion** | $C$ | Pa | $5\cdot10^{6}$ | $5\cdot10^{6}$ | $5\cdot10^{6}$ | $5\cdot10^{6}$ |
| **Internal friction coefficient (unweakened)** | $f$ | ◦ | 30 | 30 | 30 | 30 |
| **Strain weakening interval** | - | - | [0,1] | [0,1] | [0,1] | [0,1] |
| **Strain weakening factor** | $a$ | - | 0.25 | 0.25 | 0.25 | 1.0 |
| **Creep properties** | | | Wet quartzite[58] | Wet quartzite[59] | Dry olivine[60] | Wet olivine[60] |
| **Stress exponent (dis)** | $n$ | - | 4.0 | 3.0 | 3.5 | 3.5 |
| **Prefactor (dis)** | $A_{dis}$ | $Pa^{-n}\ s^{-1}$ | $8.57\cdot10^{-28}$ | $7.13\cdot10^{-18}$ | $6.52\cdot10^{-16}$ | $2.12\cdot10^{-15}$ |
| **Activation energy (dis)** | $E_{dis}$ | $J\ mol^{-1}$ | $223\cdot10^{3}$ | $345\cdot10^{3}$ | $530\cdot10^{3}$ | $480\cdot10^{3}$ |
| **Activation volume (dis)** | $V_{dis}$ | $m^3\ mol^{-1}$ | 0 | $38\cdot10^{-6}$ | $18\cdot10^{-6}$ | $11\cdot10^{-6}$ |
| **Prefactor (diff)** | $A_{diff}$ | $Pa^{-1}\ s^{-1}$ | $5.79\cdot10^{-19}$ | $2.99\cdot10^{-25}$ | $2.25\cdot10^{-9}$ | $1.5\cdot10^{-9}$ |
| **Activation energy (diff)** | $E_{diff}$ | $J\ mol^{-1}$ | $223\cdot10^{3}$ | $159\cdot10^{3}$ | $375\cdot10^{3}$ | $335\cdot10^{3}$ |
| **Activation volume (diff)** | $V_{diff}$ | $m^3\ mol^{-1}$ | 0 | $38\cdot10^{-6}$ | $6\cdot10^{-6}$ | $4\cdot10^{-6}$ |
| **Grain size (diff)** | $d$ | m | 0.001 | 0.001 | 0.001 | 0.001 |
| **Grain size exponent (diff)** | $m$ | - | 2.0 | 3.0 | 0 | 0 |